Electron-localization-resolved rotation of D_2^+ in a strong midinfrared laser pulse

Liang Xu[1] and Feng He[1,2,*]

[1]*Key Laboratory for Laser Plasmas (Ministry of Education) and School of Physics and Astronomy, Shanghai Jiao Tong University, Shanghai 200240, China*

[2]*Collaborative Innovation Center of IFSA (CICIFSA), Shanghai Jiao Tong University, Shanghai 200240, China*

(Received 4 December 2019; accepted 20 July 2020; published 6 August 2020)

Electrons have much shorter timescales of movement than nuclei, and thus electron dynamics is generally averaged out in the study of molecular rotation. However, our numerical study shows that the electron dynamical localization on different nuclei during the molecular dissociation may determine the molecular rotation directions. Taking D_2^+ as the prototype, an isolated linearly polarized attosecond pulse initiates the molecular dissociation, and then a time-delayed linearly polarized middle-infrared pulse, with the polarization cross angle $\pi/4$ to the attosecond pulse, exerts opposite torques on the molecule when the electron localizes on different nuclei, resulting in the clockwise or counterclockwise rotation of the dissociating D_2^+. The time-dependent analysis explores the complex behavior of molecular rotation determined by the ultrafast electron dynamics, and sheds light on quantum control of molecular rotation.

DOI: 10.1103/PhysRevA.102.023106

I. INTRODUCTION

The quantum control of molecular rotation [1–3] has been extensively studied with the advent of ultrafast laser technologies. Molecular rotation determines molecular alignment, which is a preparation step for further studies of molecular ultrafast processes in strong laser fields, such as high harmonic generation, molecular ionization, and dissociation. For example, by aligning molecules along different directions in advance, the linearly polarized probe laser pulse may produce alignment-dependent high-order-harmonic generation [4–7] or ionization probabilities [8–12]. Molecular rotation may induce doppler shift imprinted on the high harmonic generation [13,14] and, inversely, the high harmonic generation can be used to directly image the molecular rotation [14,15]. Rotational selective excitation can steer chemical reaction channels and the angular distribution of outgoing fragments in molecular dissociation [16–18]. Air lasing was believed to be strongly affected by rotational wave packets of the excited electronic state [19–21]. Molecular alignment also plays crucial roles for understanding complex molecular structures and attosecond transient absorption spectra [22]. Very recently, molecular echo was demonstrated in the molecular rotational wave packet [23,24].

Over the last few decades, the dissociation of hydrogen molecular ions exposed to laser fields from ultraviolet to near-infrared regions has been extensively studied and various strong-field dissociation mechanisms have been observed [25]. The scenario is quite different if the midinfrared (MIR) pulse is used. Some questions about this subject have been explored in the previous studies. For example, Chin *et al.* measured the kinetic energy of the dissociated fragments of H_2^+ and D_2^+ in the strong 10 μm laser field [26–28] and found that the proton spectrum exhibited one fairly broad distribution, whereas for the deuteron spectrum, two peaks were observed. A semiclassical approach including two electronic states was introduced by Thachuk *et al.* to successfully describe the intense-field above-threshold dissociation in the long-wavelength limit [29,30]. Mulyukov *et al.* calculated the threshold intensities for dissociation of H_2^+ from some vibrational levels in a strong low-frequency ac field and compared their results with those measured by Chin *et al.* [31]. Dietrich *et al.* developed a quantitative physical model of H_2^+ in intense MIR laser fields to study how laser-induced electron motion influences the nuclear dynamics [32]. Atabek *et al.* studied theoretically dynamical dissociation quenching of H_2^+ and HD^+ in the low-frequency regime and discussed the effects of molecular rotations and misalignments [33–35]. Paci *et al.* modified the dissociation adiabaticity parameter and assessed its utility in the interpretation of kinetic-energy distributions in the H_2^+ dissociation [36]. Under the THz light field, the numerical simulation shows that the momentum of the nuclear wave packet is periodically modulated and the modulation depth is related to the laser vector potential [37]. In addition, tunneling dissociation and nuclear rescattering were also observed theoretically by using the MIR laser pulse [38]. Besides the aforementioned studies, we wonder how an MIR laser pulse influences the molecular rotation since the molecular rotation plays a significant role in the strong-field physics domain.

For small molecules, molecular rotation can be usually untangled from the nuclear vibration and electron excitation because of its long timescale. To study the electron dynamics or nuclear vibration, one may prealign molecules, though this is unnecessary in the momentum-coincidence experiment [39], and the molecular rotation is assumed frozen when a probe pulse irradiates the molecules. Such a treatment significantly simplifies the theoretical efforts. However, for the dissociating D_2^+ under MIR pulses, the dipoles induced by

*fhe@sjtu.edu.cn

electron localization will interact with laser fields and the molecule rotates. Lately, Shao *et al.* measured the fragment momentum distributions during the D_2^+ dissociation and found that molecular rotation is important even in a strong 800 nm elliptically polarized laser pulse [40]. Then, Gong *et al.* also observed experimentally the H_2^+ molecular rotation based on the transfer of the photon spin angular momentum to nuclear orbital angular momentum [41].

Besides the coupling of the vibration and rotation, in this paper, we observe the opposite rotation of D_2^+ in a laser field. By numerically simulating the time-dependent Schrödinger equation (TDSE), we design a strategy to observe the coupling of electron excitation and molecular rotation. After the single attosecond pulse triggers the dissociation of D_2^+, the time-delayed MIR laser pulse strongly couples the $1s\sigma_g$ and $2p\sigma_u$ states, and thus the electron localizes on two nuclei unequally. Please note that the attosecond-pump-femtosecond-probe strategy has been used widely in the ultrafast community [42]. For the states with opposite electron localization, the MIR field exerts opposite torques on the dissociating D_2^+, leading to the clockwise or counterclockwise molecular rotation. Once the laser field changes its direction, the molecular rotation also reverses. The ultimate molecular rotation is the net contribution of the back-and-forth rotation induced by all different half optical cycles. The rest of the paper is organized as follows. In Sec. II, we introduce the numerical method, and the simulation results and discussions are given in Sec. III. The paper ends with a conclusion in Sec. IV.

II. NUMERICAL METHODS

We use D_2^+ as a prototype, whose molecular wave packet under the Born-Oppenheimer approximation is expressed as

$$\psi(\mathbf{r},\mathbf{R};t)=\chi_g(\mathbf{R},t)\varphi_g(\mathbf{r},\mathbf{R})+\chi_u(\mathbf{R},t)\varphi_u(\mathbf{r},\mathbf{R}), \quad (1)$$

where $\mathbf{r}$ is the electronic coordinate and $\mathbf{R}$ is the internuclear displacement, respectively. $\varphi_g(\mathbf{r},\mathbf{R})$ and $\varphi_u(\mathbf{r},\mathbf{R})$ denote the orthogonal $1s\sigma_g$ and $2p\sigma_u$ electronic states, respectively. Other highly excited electronic states have been neglected, which is reasonable since those states are far above in the energy diagram and weakly couple with the two lowest electronic states for the laser parameters used in this paper. The time evolution of the nuclear rovibrational states $\chi_g(\mathbf{R},t)$ and $\chi_u(\mathbf{R},t)$ associated with the ground and the first-excited electronic state is governed by the TDSE (Hartree atomic units are used unless stated otherwise),

$$i\frac{\partial}{\partial t}\begin{pmatrix}\chi_g(\mathbf{R},t)\\ \chi_u(\mathbf{R},t)\end{pmatrix}=(H_0+H_I(t))\begin{pmatrix}\chi_g(\mathbf{R},t)\\ \chi_u(\mathbf{R},t)\end{pmatrix}, \quad (2)$$

where the field-free Hamiltonian is written as

$$H_0=\begin{pmatrix}\frac{\mathbf{P}_R^2}{2M}+V_g(\mathbf{R}) & 0\\ 0 & \frac{\mathbf{P}_R^2}{2M}+V_u(\mathbf{R})\end{pmatrix}. \quad (3)$$

Here, $M=1836$ a.u. is the reduced nuclear mass of D_2^+, and $\mathbf{P}_R$ is the nuclear momentum operator. $V_g(\mathbf{R})$ and $V_u(\mathbf{R})$ are the isotropy potential surfaces of the $1s\sigma_g$ and $2p\sigma_u$ states [43], respectively, as shown in Figs. 2(a) and 2(c). The interaction

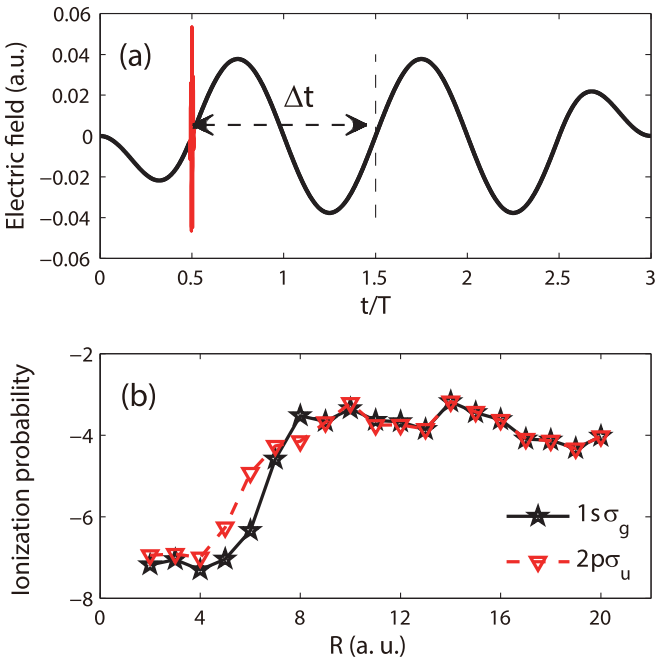

FIG. 1. (a) The electric field of the combined attosecond (red) and MIR (black) laser pulses with delay Δt. Note that their polarization directions have a cross angle $\pi/4$. (b) Ionization probabilities only induced by the MIR pulse as a function of internuclear distance for the initial states $1s\sigma_g$ and $2p\sigma_u$, respectively. The wavelength is 15 μm and the intensity is 5×10^{13} W/cm^2.

Hamiltonian is expressed as

$$H_I(t)=\begin{pmatrix}0 & \mathbf{D}(\mathbf{R})\cdot\mathbf{E}(t)\\ \mathbf{D}(\mathbf{R})\cdot\mathbf{E}(t) & 0\end{pmatrix}, \quad (4)$$

where $\mathbf{D}(\mathbf{R})=\langle\varphi_g(\mathbf{r},\mathbf{R})|\,\mathbf{r}\,|\varphi_u(\mathbf{r},\mathbf{R})\rangle$ expresses the transition dipole moment between the $1s\sigma_g$ and $2p\sigma_u$ electronic states, which is taken from Ref. [44], and $\mathbf{E}(t)$ is the laser electric field implemented in the following simulations.

Figure 1(a) shows the laser parameters in our strategy. We first use a linearly polarized attosecond pulse to induce the molecular dissociation along the $2p\sigma_u$ potential surface, and then introduce a time-delayed linearly polarized MIR laser pulse, with the cross angle $\pi/4$ between two polarization directions, to wrench the dissociating D_2^+, resulting in the molecular rotation in the plane constructed by both polarization directions. The first attosecond laser and the time-delayed MIR laser pulses are written as

$$\mathbf{E}_{\rm as}(t)=E_1 f_1(t)\sin(\omega_1 t)\hat{\mathbf{e}}_\mathbf{x} \quad (5)$$

and

$$\mathbf{E}_{\rm MIR}(t)=E_2 f_2(t-\Delta t)\sin(\omega_2 t-\omega_2\Delta t)(\hat{\mathbf{e}}_\mathbf{x}+\hat{\mathbf{e}}_\mathbf{y}). \quad (6)$$

Here the former has the $\sin^2$ profile $f_1(t)$ with the pulse width of four optical cycles, and the latter is a trapezoid envelope $f_2(t-\Delta t)$ with one optical cycle for ramp on and off, and two optical cycles for the plateau. The time delay Δt is variable in different calculations. The attosecond pulse has the wavelength $\lambda_1=106$ nm (angular frequency $\omega_1=0.43$ a.u.) and the intensity $I_1=1.0\times10^{14}$ W/cm^2 (field amplitude $E_1=0.0534$ a.u.). The MIR pulse has the wavelength $\lambda_2=15$ μm

(angular frequency $\omega_2 = 3.04 \times 10^{-3}$ a.u.) and intensity $I_2 = 5.0 \times 10^{13}$ W/cm^2 (field amplitude $E_2 = 0.0267$ a.u.). Its period is defined as $T \approx 50$ fs. For a negative (positive) time delay Δt, the attosecond pulse precedes (lags behind) the MIR pulse.

In our calculations, $\mathbf{R}$ is confined in the plane constructed by the two polarization directions. Equation (2) is solved using a second-order split-operator method with the time step $\delta t = 0.1$ a.u., and combined with a three-point finite-difference method in the spatial steps $\delta R_x = \delta R_y = 0.02$ a.u. [45]. The initial state is obtained by the imaginary-time propagation, and the wave-function propagation in real time is solved using the Crank-Nicholson method. The two-dimensional spatial area covers the space $-120 < R_x < 120$ a.u. and $-120 < R_y < 120$ a.u.. Such a numerical box is big enough to hold all dissociative wave packets during the simulation. Therefore, no absorbers in boundaries are needed. The dissociative wave packets in momentum representation $\widetilde{\chi}_g(\mathbf{P}_\mathrm{R})$ and $\widetilde{\chi}_u(\mathbf{P}_\mathrm{R})$ are obtained by Fourier transforming $\chi_g(\mathbf{R}, t_f)$ and $\chi_u(\mathbf{R}, t_f)$ in the range of $R > 10$ a.u. at the terminal time t_f, where R is the internuclear distance. The overall nuclear momentum distribution is obtained via $W_{g+u}(\mathbf{P}_\mathrm{R}) = |\widetilde{\chi}_g(\mathbf{P}_\mathrm{R})|^2 + |\widetilde{\chi}_u(\mathbf{P}_\mathrm{R})|^2$. The convergence of the calculations has been tested by using finer spatial and time steps, whereas almost identical results were obtained.

Before studying the molecular rotation, we first verify the reliability of the numerical model, i.e., proving the feasibility of neglecting the ionization. We calculate the ionization probability of D_2^+ with the fixed-nuclei approximation. The polarization direction of the laser field is parallel to the molecular axis, and then the system keeps the rotational symmetry. We thus adopt the three-dimensional cylindrical coordinate (ρ, z) to describe the electron ionization [46]. The field-free Hamiltonian of D_2^+ is given in the following form:

$$H_0 = -\frac{1}{2}\left(\frac{\partial^2}{\partial\rho^2} + \frac{1}{\rho}\frac{\partial}{\partial\rho} + \frac{\partial^2}{\partial z^2}\right) - \frac{1}{\sqrt{(z - R/2)^2 + \rho^2}} - \frac{1}{\sqrt{(z + R/2)^2 + \rho^2}}, \quad (7)$$

where D_2^+ is oriented along the z axis. The interaction of the electron with the laser field is written in the dipole approximation and length gauge as

$$V(t) = zE(t). \quad (8)$$

We numerically simulate the above TDSE also using the difference Crank-Nicholson method with a time step of $\delta t = 0.05$ a.u. The grid ranges in the ρ dimension from 0 to 20 a.u. and for z from -30 to 30 a.u. with 200 and 600 points in the two directions, respectively. To suppress the unphysical reflection from boundaries, a $\cos^{1/8}$ masking function has been adopted. The initial state ($1s\sigma_g$ or $2p\sigma_u$) has been obtained using imaginary-time propagation, respectively. After the laser field finishes, we keep propagating the wave packets until the ionized signals all are absorbed. By counting on the probability of bound states, one may directly get the ionization probability since all probability is conserved. For the MIR laser pulse as mentioned above, the maximum ionization probability appears at $R \approx 14$ a.u. and is less than 1.0×10^{-2} for D_2^+ either in the $1s\sigma_g$ or $2p\sigma_u$ state. The charge-resonance enhanced ionization is clearly observed when the internuclear distance is in the range $6 < R < 15$ a.u. [47–49], as shown in Fig. 1(b). Hence, the total ionization is negligible even though the evolution of the nuclear wave packet is involved and the two-state model is proper to study the dissociation of D_2^+ under the laser parameters used in this paper.

III. RESULTS AND DISCUSSIONS

The dissociation triggered solely by an isolated attosecond pulse with the wavelength 106 nm has been well understood [50]. In that case, D_2^+ is resonantly excited from the $1s\sigma_g$ to the $2p\sigma_u$ state, and then dissociates along the $2p\sigma_u$ potential surface, ending with the nuclear energy peaked at about 9.0 eV and the electron equally distributes on two nuclei. During the dissociation, if a MIR laser pulse is introduced, the dissociation process becomes complex. Since the optical period ($T \approx 50$ fs) of the MIR laser is comparable to the timescale of the nuclear movement, the dissociating D_2^+ sees the adiabatic change of the electric field, and thus we investigate the nuclear dynamics in the field-dressed representation. Hence, we analyze the nuclear wave-packet propagation on the adiabatic $V_\pm(\mathbf{R}, t)$ potential curves [37,51,52], which are expressed as

$$V_\pm(\mathbf{R}, t) = \frac{V_g(\mathbf{R}) + V_u(\mathbf{R})}{2} \pm \sqrt{\frac{[V_g(\mathbf{R}) - V_u(\mathbf{R})]^2}{4} + [\mathbf{D}(\mathbf{R}) \cdot \mathbf{E}(t)]^2}. \quad (9)$$

The corresponding two instantaneous eigenstates of $V_\pm(\mathbf{R}, t)$ are

$$\chi_-(\mathbf{R}, t) = \cos(\alpha)\chi_g(\mathbf{R}, t) + \sin(\alpha)\chi_u(\mathbf{R}, t) \quad (10)$$

and

$$\chi_+(\mathbf{R}, t) = -\sin(\alpha)\chi_g(\mathbf{R}, t) + \cos(\alpha)\chi_u(\mathbf{R}, t), \quad (11)$$

where α satisfies

$$\tan(2\alpha) = -2[\mathbf{D}(\mathbf{R}) \cdot \mathbf{E}(t)]/[V_u(\mathbf{R}) - V_g(\mathbf{R})]. \quad (12)$$

Here, α tends to be zero when R is small or the temporary electric field vanishes, in which case $\chi_+(\mathbf{R}, t) = \chi_u(\mathbf{R}, t)$ and $\chi_-(\mathbf{R}, t) = \chi_g(\mathbf{R}, t)$. If R is large, for example, $R > 10$ a.u., $V_g(\mathbf{R})$ and $V_u(\mathbf{R})$ are nearly degenerate and thus α switches between $\pm\pi/4$ when the temporary electric field reverses its direction, resulting in the swap of $\chi_+(\mathbf{R}, t)$ and $\chi_-(\mathbf{R}, t)$. Figures 2(b) and 2(d) show the distorted potential surfaces $V_\pm(\mathbf{R}, t)$ when the instantaneous electric field is 5.0×10^{13} W/cm^2, and the temporary electric field points to the direction with the cross angle $\pi/4$ to the x axis. In the direction of the laser field, the potential surfaces are distorted most severely. $V_+(\mathbf{R}, t)$ is lifted and $V_-(\mathbf{R}, t)$ is downpressed. In the $V_+(\mathbf{R}, t)$ surface, a valley is formed in the perpendicular direction of the electric field, whereas $V_-(\mathbf{R}, t)$ forms a local maximum in the same direction.

We now study the rotation of the dissociating D_2^+. After the attosecond laser pulse induces the dissociation, the time-delayed linearly polarized MIR laser pulse expressed by Eq. (6) is introduced to wrench the dissociating D_2^+. The converged nuclear momentum distributions depend on the

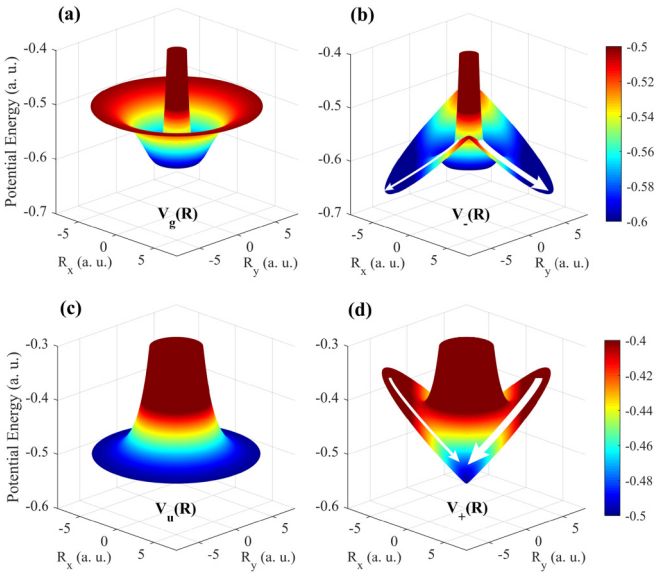

FIG. 2. The potential-energy surfaces of (a) $V_g(\mathbf{R})$, (b) $V_-(\mathbf{R},t)$, (c) $V_u(\mathbf{R})$, and (d) $V_+(\mathbf{R},t)$. The temporary electric field of the MIR pulse is $I_2 = 5.0 \times 10^{13}$ W/cm^2, and points to the direction $\theta = \pi/4$. The dissociation is triggered by the x-axis linearly polarized attosecond pulse with the wavelength 106 nm. The white arrows denote the wave-packet flow directions, and the thicker ones indicate larger wave-packet probabilities in the corresponding sectors.

time delay between two pulses, as shown in Figs. 3(b) and 3(c) for $\Delta t = -0.3T$ and $-0.66T$, respectively. For comparison, we also give the results without the MIR pulse, as depicted in Fig. 3(a). In all three panels of Fig. 3, the same black dashed circle with the radius $|\mathbf{p}_0| = \sqrt{2M[V_u(R_0) + 0.5]}$ is presented for referencing the nuclear momentum. Here, $R_0 = 2$ a.u. is the equilibrium internuclear distance for D_2^+ in the ground state, and $V_u(R_0)$ is the $2p\sigma_u$ potential energy at $R = R_0$. In the centers of Figs. 3(b) and 3(c), the signals with very low momenta and few probabilities are purely induced by the MIR field, which is not discussed in this paper. We focus on the fragments induced by the attosecond pulse and wrenched by the MIR field. In Fig. 3(b), the nuclear momenta almost sit inside the black dashed circle, which means the dissociative fragments finally lose energies if the MIR field is introduced at $\Delta t = -0.3T$. While in the case of $\Delta t = -0.66T$, as shown in Fig. 3(c), the circle divides the nuclear momentum distributions into two parts, i.e., the inner part with small nuclear momenta and the outer part with larger nuclear momenta. Such a delay-dependent nuclear momentum distribution can be approximately formulated as $\mathbf{p_R} = \mathbf{p}_0 \pm \mathbf{A}(t_0)/2$ [37], where t_0 is the time when the internuclear distance approaches $R = 10$ a.u., and $\mathbf{A}(t_0)$ is the vector potential of the MIR pulse at t_0. Note that here, $R = 10$ a.u. only means the internuclear distance where the $1s\sigma_g$ and $2p\sigma_u$ states just become degenerate, and hence R is not strictly required to be exactly 10 a.u.. The small variation of R does not change our interpretation. The physical meaning of this expression can be understood as the MIR streaking of the nuclear momentum. For $\Delta t = -0.3T$, the MIR laser vector potential is about 4.0 when the internuclear distance becomes 10 a.u., whereas the corresponding MIR laser vector potential $\mathbf{A}(t_0)$ is about -12.4 a.u. for $\Delta t = -0.66T$.

Besides the streaking of nuclear momenta, Figs. 3(b) and 3(c) present the molecular rotation. Since the dissociation is triggered by the x-axis linearly polarized attosecond pulse, two nodes should appear at the vertical axis exactly if without molecular rotation during the dissociation, as shown in Fig. 3(a). However, as marked by the vertical dash-dotted lines in Figs. 3(b) and 3(c), the nodes deviate from the vertical axis, which is the evidence of the molecular rotation. More interestingly, as shown in Fig. 3(c), the inner and outer parts rotate oppositely, though they experience the same MIR field, and their rotational angles are 6.67 and -8.67 degrees, respectively; while in Fig. 3(b), the rotation angle of the whole wave packet is about -5.0 degrees.

The molecular rotation can be understood by tracing the wave-packet propagation on $V_\pm(\mathbf{R},t)$ potential surfaces. $\chi_\pm(\mathbf{R},t)$ tend to align along the direction $\theta = \mp\pi/4$, respectively, since $V_\pm(\mathbf{R},t)$ have the local minima in these two orthogonal directions. Because the attosecond pulse is polarized along the x axis, the dissociative probability in the sector $|\theta| < \pi/4$ dominates over that in $\pi/4 < |\theta| <$

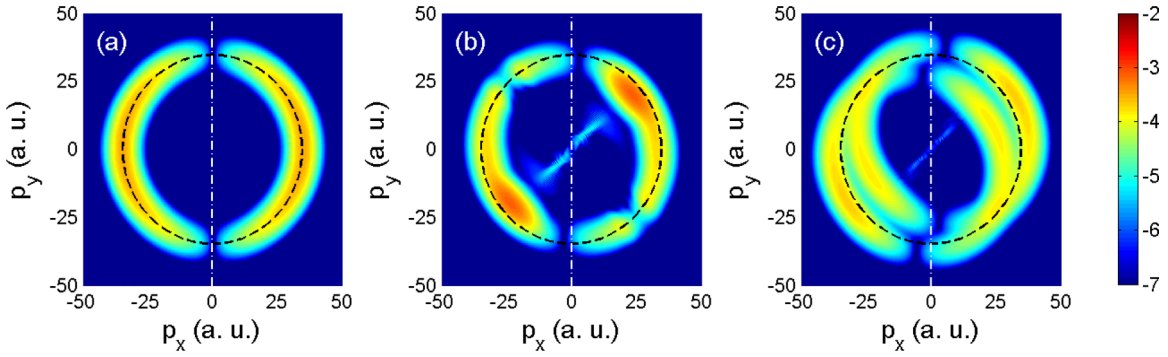

FIG. 3. The converged nuclear momentum distribution (a) without the MIR pulse as well as when the time delay is (b) $\Delta t = -0.3T$ and (c) $\Delta t = -0.66T$. The intensities of the attosecond ($\lambda_1 = 106$ nm) and MIR ($\lambda_2 = 15$ μm) pulses are $I_1 = 1.0 \times 10^{14}$ W/cm^2 and $I_2 = 5.0 \times 10^{13}$ W/cm^2. The black dashed circles in the three panels express the expected classical nuclear momenta in the case that the MIR field is not introduced.

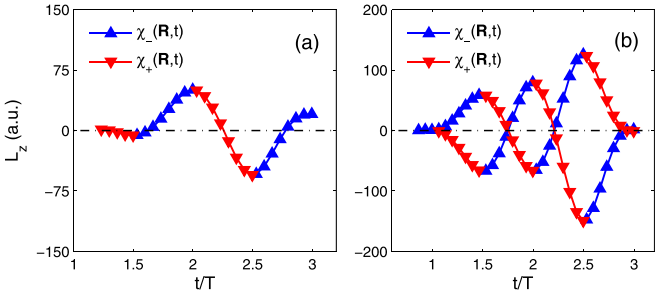

FIG. 4. The angular momenta $\langle L_z^{\pm}(t)\rangle$ of the dissociative nuclear wave packet $\chi_{\pm}(\mathbf{R},t)$ as a function of the time when the time delay is (a) $\Delta t=-0.3T$ and (b) $\Delta t=-0.66T$. The laser parameters are the same as those used in Figs. 3(b) and 3(c).

$3\pi/4$. Though $\chi_+(\mathbf{R},t)$ tends to align along the direction $\theta=-\pi/4$, as marked by the arrows in Fig. 2(d), the expected rotation angle for $\chi_+(\mathbf{R},t)$ is negative, i.e., the wave packet on $V_+(\mathbf{R},t)$ rotates clockwise. On the contrary, the wave packet on $V_-(\mathbf{R},t)$ rotates counterclockwise, as indicated by the arrows in Fig. 2(b). In every half of an optical period, $\chi_{\pm}(\mathbf{R},t)$ swap each other. Hence, the molecule rotates back and forth with the time evolution. The final rotation angle is the summation of these back-and-forth rotations contributed by every half optical period.

Such a back-and-forth rotation can be confirmed by extracting the time-dependent angular momenta $\langle L_z^{\pm}(t)\rangle$, which are calculated via

$$\langle L_z^{\pm}(t)\rangle=\frac{\langle\chi_{\pm}(\mathbf{R},t)|\mathbf{R}\times\mathbf{p_R}|\chi_{\pm}(\mathbf{R},t)\rangle}{\langle\chi_{\pm}(\mathbf{R},t)|\chi_{\pm}(\mathbf{R},t)\rangle}. \tag{13}$$

Figures 4(a) and 4(b) show the time-dependent angular momenta $\langle L_z^{\pm}(t)\rangle$ for the cases of $\Delta t=-0.3T$ and $-0.66T$, respectively. For a proper time delay, for example, $\Delta t=-0.3T$, $\chi_u(\mathbf{R},t)$ happens to become pure $\chi_+(\mathbf{R},t)$ when the internuclear distance approaches 10 a.u.. In the later time, the molecule is always in the temporary eigenstate, either $\chi_+(\mathbf{R},t)$ or $\chi_-(\mathbf{R},t)$. This is why there is only one donut of the nuclear momentum distribution in Fig. 3(b). As shown in Fig. 4(a), the angular momentum oscillates with the period of $T/2$. For another time delay of $\Delta t=-0.66T$, $\chi_u(\mathbf{R},t)$, induced initially by the attosecond pulse, changes into the superimposed states of $\chi_+(\mathbf{R},t)$ and $\chi_-(\mathbf{R},t)$ when the internuclear distance approaches 10 a.u.. Thus, in any later time, the molecule is always in the superimposed state $\chi_{\pm}(\mathbf{R},t)$, who swap each other once the laser field changes its direction. During this process, $\mathrm{V}_+(\mathbf{R},t)$ makes the dissociating wave packet $\chi_+(\mathbf{R},t)$ decelerate and $\mathrm{V}_-(\mathbf{R},t)$ accelerates $\chi_-(\mathbf{R},t)$, so two radial donuts appear in the nuclear momentum distribution. The angular momenta of $\chi_{\pm}(\mathbf{R},t)$ are opposite and oscillate with the period of $T/2$, as shown in Fig. 4(b). According to the angular momentum conservation, the very large value of $\langle L_z^{\pm}(t)\rangle$ (for example, up to 100) means more than 100 MIR photons participate in the interaction.

The molecular rotation can also be understood in view of different electron localization. We define the nuclear wave packets $\chi_{l/r}(\mathbf{R},t)=[\chi_g(\mathbf{R},t)\mp\chi_u(\mathbf{R},t)]/\sqrt{2}$ representing the electron localization on the left or right nucleus as done in the one-dimensional case [50,53]. According to Eqs. (10)–(12), if the temporary laser field points to the direction $\theta=\pi/4$, the electron in the sector $-\pi/4<\theta<3\pi/4$ in $\chi_+(\mathbf{R},t)$ localizes on the right nucleus, which is expressed as $\chi_+^r(\mathbf{R},t)$. However, the other half plane of $\chi_+(\mathbf{R},t)$ has the electron localization on the left one, i.e., $\chi_l^+(\mathbf{R},t)$. Intuitively, in the same sector, $\chi_-(\mathbf{R},t)$ has the opposite electron localization $\chi_l^-(\mathbf{R},t)$ and $\chi_r^-(\mathbf{R},t)$ to $\chi_+(\mathbf{R},t)$. The localization asymmetry for $\chi_{\pm}(\mathbf{R},t)$ is defined as $A_{\pm}(\mathbf{R},t)=[|\chi_{\pm}^l(\mathbf{R},t)|^2-|\chi_{\pm}^r(\mathbf{R},t)|^2]/[|\chi_{\pm}^l(\mathbf{R},t)|^2+|\chi_{\pm}^r(\mathbf{R},t)|^2]$ [50,53]. For D_2^+ with a specific electron localization, it is analogous to a classical rotor. The expected torque exerting on $\chi_{\pm}(\mathbf{R},t)$ is expressed as $\mathbf{M}_{\pm}(t)\propto\int A_{\pm}(\mathbf{R},t)\mathbf{D}(\mathbf{R})\times\mathbf{E}(t)d\mathbf{R}$ [40], where $\mathbf{D}(\mathbf{R})$ is approximately equal to $\mathbf{R}/2$. If the laser field changes its direction, the torque also reverses, and thus the molecule swings in the plane constructed by the two polarization directions of the two pulses, which coincides with the analysis of time-dependent angular momenta shown in Fig. 4. We note that the explanations based on the wave-function propagation on $V_{\pm}(\mathbf{R},t)$ and on the electron localization are fundamentally the same.

To observe the localization-resolved molecular rotation, the carrier-envelope-phase-stabilized strong laser field is necessary. Based on the simulation results, an MIR pulse with the wavelength longer than 5 μm and the intensity higher than 10^{13} W/cm^2 is required to resolve the inner and outer rings shown in Fig. 3(c). Though such an MIR laser pulse is not in hand yet, some strategies have been proposed to produce such an MIR pulse [54–56], and thus make it possible to experimentally observe the predicted phenomena in coming years. In our strategy, the pump pulse is not necessarily as short as attoseconds. If the duration of the pump pulse is shorter than half a period of the time-delayed MIR pulse, the nuclear streaking can be observed clearly. Generally speaking, a lighter molecule, such as H_2^+, is favored to observe such opposite rotation in MIR fields. The rotation might not be distinct if a very heavy molecule is used even though the electron can be localized on the selective nucleus.

IV. CONCLUSIONS

To summarize, we have revealed the pathway-resolved rotation of the dissociating D_2^+ via numerically simulating the TDSE. In our strategy, the dissociating nuclear wave packet induced by the attosecond pulse is wrenched by the 15 μm MIR pulse. The MIR-distorted potential surfaces $V_{\pm}(\mathbf{R},t)$ have minima in two orthogonal directions, and thus the nuclear wave packets propagating along $V_{\pm}(\mathbf{R},t)$ tend to rotate in opposite directions. In every half optical period, $\chi_{\pm}(\mathbf{R},t)$ swap each other, and the molecule reverses its rotation direction. The dynamical rotation can also be understood based on the electron localization. When the electron localizes on different nuclei, the formed dipoles have opposite directions, and thus the same laser electric field exerts opposite torques on the molecule, resulting in the clockwise and counterclockwise rotation. Finally, the molecule dissociating along different pathways or having different electron localization acquires different rotation angles. Our study shows that the electron excitation dynamics may play important roles in molecular rotation.

ACKNOWLEDGMENTS

This work was supported by the National Key R&D Program of China (Grant No. 2018YFA0404802), Innovation Program of Shanghai Municipal Education Commission(Grant No. 2017-01-07-00-02-E00034), National Natural Science Foundation of China (NSFC) (Grants No. 11574205, No. 11721091, No. 91850203), and Shanghai Shuguang Project (Grant No. 17SG10). Simulations were performed on the π supercomputer at Shanghai Jiao Tong University.

[1] H. Stapelfeldt and T. Seideman, Rev. Mod. Phys. **75**, 543 (2003).

[2] T. Seideman and E. Hamilton, Adv. At. Mol. Opt. Phys. **52**, 289 (2005).

[3] C. P. Koch, M. Lemeshko, and D. Sugny, Rev. Mod. Phys. **91**, 035005 (2019).

[4] D. G. Lappas and J. P. Marangos, J. Phys. B: At. Mol. Opt. Phys. **33**, 4679 (2000).

[5] R. Velotta, N. Hay, M. B. Mason, M. Castillejo, and J. P. Marangos, Phys. Rev. Lett. **87**, 183901 (2001).

[6] M. Lein, N. Hay, R. Velotta, J. P. Marangos, and P. L. Knight, Phys. Rev. Lett. **88**, 183903 (2002).

[7] T. Kanai, S. Minemoto, and H. Sakai, Nature (London) **435**, 470 (2005).

[8] M. Plummer and J. F. McCann, J. Phys. B: At. Mol. Opt. Phys. **30**, L401 (1997).

[9] I. V. Litvinyuk, K. F. Lee, P. W. Dooley, D. M. Rayner, D. M. Villeneuve, and P. B. Corkum, Phys. Rev. Lett. **90**, 233003 (2003).

[10] D. Pavičić, K. F. Lee, D. M. Rayner, P. B. Corkum, and D. M. Villeneuve, Phys. Rev. Lett. **98**, 243001 (2007).

[11] S. F. Zhao, C. Jin, A.-T. Le, T. F. Jiang, and C. D. Lin, Phys. Rev. A **81**, 033423 (2010).

[12] L. B. Madsen, O. I. Tolstikhin, and T. Morishita, Phys. Rev. A **85**, 053404 (2012).

[13] O. Faucher, E. Prost, E. Hertz, F. Billard, B. Lavorel, A. A. Milner, V. A. Milner, J. Zyss, and I. S. Averbukh, Phys. Rev. A **94**, 051402(R) (2016).

[14] L. X. He, P. F. Lan, A.-T. Le, B. N. Wang, B. C. Wang, X. S. Zhu, P. X. Lu, and C. D. Lin, Phys. Rev. Lett. **121**, 163201 (2018).

[15] Y. Q. He, L. X. He, P. F. Lan, B. N. Wang, L. Li, X. S. Zhu, W. Cao, and P. X. Lu, Phys. Rev. A **99**, 053419 (2019).

[16] J. J. Larsen, I. Wendt-Larsen, and H. Stapelfeldt, Phys. Rev. Lett. **83**, 1123 (1999).

[17] T. P. Rakitzis, A. J. van den Brom, and M. H. M. Janssen, Science **303**, 1852 (2004).

[18] M. McDonald, B. H. McGuyer, F. Apfelbeck, C.-H. Lee, I. Majewska, R. Moszynski, and T. Zelevinsky, Nature (London) **535**, 122 (2016).

[19] H. S. Zhang, C. R. Jing, J. P. Yao, G. H. Li, B. Zeng, W. Chu, J. L. Ni, H. Q. Xie, H. L. Xu, S. L. Chin *et al.*, Phys. Rev. X **3**, 041009 (2013).

[20] A. Azarm, P. Corkum, and P. Polynkin, Phys. Rev. A **96**, 051401(R) (2017).

[21] T. Ando, E. Lötstedt, A. Iwasaki, H. L. Li, Y. Fu, S. Q. Wang, H. L. Xu, and K. Yamanouchi, Phys. Rev. Lett. **123**, 203201 (2019).

[22] J. E. Bækhøj and L. B. Madsen, Phys. Rev. A **94**, 043414 (2016).

[23] G. Karras, E. Hertz, F. Billard, B. Lavorel, J.-M. Hartmann, O. Faucher, E. Gershnabel, Y. Prior, and I. Sh. Averbukh, Phys. Rev. Lett. **114**, 153601 (2015).

[24] K. Lin, P. Lu, J. Ma, X. Gong, Q. Song, Q. Ji, W. Zhang, H. Zeng, J. Wu, G. Karras *et al.*, Phys. Rev. X **6**, 041056 (2016).

[25] A. Giusti-Suzor, F. H. Mies, L. F. DiMauro, E. Charron, and B. Yang, J. Phys. B: At. Mol. Opt. Phys. **28**, 309 (1995).

[26] F. A. Ilkov, S. Turgeon, T. D. G. Walsh, and S. L. Chin, Chem. Phys. Lett. **247**, 1 (1995).

[27] F. A. Ilkov, T. D. G. Walsh, S. Turgeon, and S. L. Chin, Phys. Rev. A **51**, R2695(R) (1995).

[28] T. D. G. Walsh, L. Strach, and S. L. Chin, J. Phys. B: At. Mol. Opt. Phys. **31**, 4853 (1998).

[29] M. Thachuk, M. Yu. Ivanov, and D. M. Wardlaw, J. Chem. Phys. **105**, 4094 (1996).

[30] M. Thachuk, M. Yu. Ivanov, and D. M. Wardlaw, J. Chem. Phys. **109**, 5747 (1998).

[31] Z. Mulyukov, M. Pont, and R. Shakeshaft, Phys. Rev. A **54**, 4299 (1996).

[32] P. Dietrich, M. Y. Ivanov, F. A. Ilkov, and P. B. Corkum, Phys. Rev. Lett. **77**, 4150 (1996).

[33] F. Châteauneuf, T.-T. Nguyen-Dang, N. Ouellet, and O. Atabek, J. Chem. Phys. **108**, 3974 (1998).

[34] H. A.-Rachid, T.-T. Nguyen-Dang, and O. Atabek, J. Chem. Phys. **110**, 4737 (1999).

[35] H. A.-Rachid, T.-T. Nguyen-Dang, and O. Atabek, J. Chem. Phys. **114**, 2197 (2001).

[36] J. T. Paci and D. M. Wardlaw, J. Chem. Phys. **119**, 7824 (2003).

[37] T. Y. Xu and F. He, Phys. Rev. A **88**, 043426 (2013).

[38] Z. C. Li, C. Ruiz, and F. He, Phys. Rev. A **90**, 033421 (2014).

[39] J. Ullrich, R. Moshammer, A. Dorn, R. Dörner, L. Ph H. Schmidt, and H. Schmidt-Böcking, Rep. Prog. Phys. **66**, 1463 (2003).

[40] Y. Shao, P. He, M. M. Liu, X. Sun, M. Li, Y. Deng, C. Wu, F. He, Q. Gong, and Y. Liu, Phys. Rev. A **95**, 031404(R) (2017).

[41] X. C. Gong, P. L. He, J. Y. Ma, W. B. Zhang, F. H. Sun, Q. Y. Ji, K. Lin, H. X. Li, J. J. Qiang, P. F. Lu *et al.*, Phys. Rev. A **99**, 063407 (2019).

[42] M. Nisoli, P. Decleva, F. Calegari, A. Palacios, and F. Martín, Chem. Rev. **117**, 10760 (2017).

[43] T. E. Sharp, At. Data. Nucl. Data. Tables **2**, 119 (1970).

[44] D. E. Ramaker and J. M. Peek, At. Data Nucl. Data Tables **5**, 167 (1973).

[45] J. Crank and P. Nicholson, Math. Proc. Camb. Phil. Soc. **43**, 50 (1947).

[46] L. Xin, H. C. Qin, W. Y. Wu, and F. He, Phys. Rev. A **92**, 063803 (2015).

[47] K. Codling, L. J. Frasinski, and P. A. Hatherly, J. Phys. B: At. Mol. Opt. Phys. **22**, L321 (1989).
[48] T. Zuo and A. D. Bandrauk, Phys. Rev. A **52**, R2511(R) (1995).
[49] T. Seideman, M. Y. Ivanov, and P. B. Corkum, Phys. Rev. Lett. **75**, 2819 (1995).
[50] F. He, C. Ruiz, and A. Becker, Phys. Rev. Lett. **99**, 083002 (2007).
[51] I. Kawata, H. Kono, and Y. Fujimura, J. Chem. Phys. **110**, 11152 (1999).
[52] F. Kelkensberg, G. Sansone, M. Y. Ivanov, and M. Vrakking, Phys. Chem. Chem. Phys. **13**, 8647 (2011).
[53] M. F. Kling, Ch. Siedschlag, A. J. Verhoef, J. I. Khan, M. Schultze, Th. Uphues, Y. Ni, M. Uiberacker, M. Drescher, F. Krausz *et al.*, Science **312**, 246 (2006).
[54] D. Haberberger, S. Tochitsky, and C. Joshi, Opt. Express **18**, 17865 (2010).
[55] I. Pupeza, D. Sánchez, J. Zhang, N. Lilienfein, M. Seidel, N. Karpowicz, T. Paasch-Colberg, I. Znakovskaya, M. Pescher, W. Schweinberger *et al.*, Nat. Photon. **9**, 721 (2015).
[56] Z. Nie, C.-H. Pai, J. Hua, C. Zhang, Y. Wu, Y. Wan, F. Li, J. Zhang, Z. Cheng, Q. Su *et al.*, Nat. Photon. **12**, 489 (2018).